Uranium removal from mining water using Cu substituted hydroxyapatite

Stephanie Szenknect, Adel Mesbah, Michael Descostes, Abdoulaye Maihatchi-Ahamed, Laura Bonato, Malvina Massonnet, Yannis Ziouane, Evelyne Vors, Thomas Vercouter, Nicolas Clavier, et al.

Uranium removal from mining water using Cu substituted hydroxyapatite

STEPHANIE SZENKNECT[*§], *ADEL MESBAH*[§], *MICHAEL DESCOSTES*[#], *ABDOULAYE MAIHATCHI-AHAMED*[§], *LAURA BONATO*[§], *MALVINA MASSONNET*[§], *YANNIS ZIOUANE*[§], *EVELYNE VORS*[‡], *THOMAS VERCOUTER*[‡], *NICOLAS CLAVIER*[§], *JOSEPH LAUTRU*[§], *NICOLAS DACHEUX*[§]

[§] ICSM, CEA, CNRS, ENSCM, Univ. Montpellier, Site de Marcoule, BP 17171, 30207 Bagnols/Cèze cedex, France

[#] ORANO Mines, R&D Dpt., Tour AREVA, 1, place Jean Millier, 92084 Paris, La Défense, France

[‡] Den – Service d'Etudes Analytiques et de Réactivité des Surfaces (SEARS), CEA, Université Paris-Saclay, F-91191, Gif sur Yvette, France

ABSTRACT

In this study, synthetic copper substituted hydroxyapatite (Cu-Hap), $Cu_xCa_{10-x}(PO_4)_6(OH)_2$ were prepared by co-precipitation method and were used as reactive materials in batch experiments to immobilize uranyl. The limit of incorporation of Cu into a single-phased Cu-Hap reached $x_{Cu} \leq 1.59$. The synthetic Cu-Hap samples obtained with various Cu contents were contacted with

synthetic uranyl doped solutions and with real mining waters showing various pH and chemical compositions. A fast and strong decrease of the uranium concentration was observed, followed by the establishment of an equilibrium after 1 to 4 days of contact with the solutions. Examination of the solid phase after uranium uptake was performed using a combination of techniques. Depending on the composition of the solution and the copper content of the Cu-Hap, various mechanisms of uranium removal were observed. Based on the experimental results and geochemical simulations, it appeared that the main interest for using Cu-Hap is to enlarge the domain of water compositions for which the precipitation of meta-torbernite, $(H_3O)_{0.4}Cu_{0.8}(UO_2)_2(PO_4)_2 \cdot 7.6\ H_2O$ is the predominant mechanism associated to the uranium removal, especially for pH > 6.7 where carbonate uranium species are predominant.

1. INTRODUCTION

Uranium ore mining, processing and manufacturing can contribute to groundwater contamination. Uranium is transported in groundwater mainly as dissolved U(VI) species, which can threaten ecosystems in the vicinity of contaminated sites. High costs associated with pump-and-treat remediation strategies and toughening of regulatory requirements regarding sewage discharge have prompted research into more effective methods[1, 2]. In this field, new methods involving hydroxyapatite (Hap) amendments to immobilize U(VI) as a nonlabile uranyl phosphate phase have been extensively studied[3-17]. The rationale for using these methods is the remarkable stability of uranyl phases of the autunite group ($M^{II}(UO_2)_2(PO_4)_2 \cdot xH_2O$ or $M^{I}_2(UO_2)_2(PO_4)_2 \cdot xH_2O$) under environmental conditions[18]. The study of natural deposits in oxidizing bedrock aquifers demonstrated that phases of the autunite group are stable for tens to hundreds thousand years[19]. Examination of the reported standard solubility products of the phases of the autunite group[20-26] shows that meta-torbernite, $(H_3O)_{0.4}Cu_{0.8}(UO_2)_2(PO_4)_2 \cdot 7.6\ H_2O$ is the less soluble one (Erreur ! Source du renvoi introuvable. of the supporting information). The ubiquity of meta-torbernite in oxidized secondary U ore deposits, contaminated sediments or mine tailings strengthen this conclusion[27].

However, the precipitation of U-phosphate phases of the autunite group is not the only mechanism of immobilization observed when using Hap as reactive material to remove uranium from contaminated solutions. Surface complexation, ion exchange[5-8, 12] and surface mineralization[28] can occur depending on the composition of the solution and the total uranium concentration,. The fluor-apatite structure can also accommodate hexavalent uranium by substitution in the Ca1 site[29]. The precipitation of chernikovite or meta-autunite is the mechanism responsible for the immobilization of uranyl either by surface precipitation following

sorption or by precipitation in the bulk solution. However, the stability of the precipitated phases could be strongly impacted by the formation of uranyl carbonates species predominant in near neutral pH and aerated groundwater, as observed by Simon et al.[12].

On the other hand, Cu-substituted hydroxyapatite (Cu-Hap) has been successfully prepared for its antimicrobial activity and biocompatibility in bioceramics used as bone implants, or for its catalytic properties in the removal of NOx issued from diesel and lean burn gasoline[30-34]. Cu-Hap was also prepared to improve the sorption capacity of the hydroxyapatite in groundwaters contaminated with arsenate[35]. Mainly two ways of synthesis were reported in the literature. The first one consisted in the synthesis of an hydroxyapatite by the classical neutralization method initially developed by Wallayes[36] followed by cation exchange step. This protocol led to the preparation of Cu-Hap samples with low Cu incorporation contents. Samples prepared with Cu molar contents higher than $x_{Cu} = 0.02$ were mixtures of phases[31, 32]. The second way of synthesis was based on the co-precipitation method[30, 34]. Shanmugam et al.[30] and Stanic et al.[34] obtained single phase Cu-Hap for $x_{Cu} < 0.53$ and for $x_{Cu} < 0.04$, respectively.

In this study, we assessed the feasibility of using synthetic Cu-Hap prepared by co-precipitation method to immobilize uranyl as stable meta-torbernite phase. The limit of incorporation of Cu into a single-phased Cu-Hap was determined, then the prepared samples were used as reactive materials in batch experiments. The synthetic Cu-Hap samples obtained with various Cu contents were contacted with synthetic uranyl doped solutions and with real mining waters showing various pH and chemical compositions, thus different uranium speciation in solution. The performance of the Cu-Hap was analyzed and compared to Hap based on the rate and extent of uranium sequestration. The mechanism of immobilization was investigated

with respect to various conditions tested through geochemical calculations and solid phase characterizations.

2. MATERIALS AND METHODS

2.1. Synthesis of Cu substituted Hap

Copper substituted hydroxyapatite, $Cu_xCa_{10-x}(PO_4)_6(OH)_2$ was precipitated by neutralization of 200 mL of a solution prepared by dissolving $Cu(OH)_2$ in 0.12 M H_3PO_4 (Solution A) Sigma-Aldrich, analytical grade, Carlo Erba, ACS reagent) with 0.4 M $Ca(OH)_2$ (solution B) (Sigma Aldrich, ACS reagent). The weighted amount of $Cu(OH)_2$ was adjusted to reach the desired concentration of copper in the solution A: $C_{Cu}= 0.02\times x_{Cu}$ M. A defined volume of solution B was added considering the final stoichiometry of Cu-Hap. Solution A was heated at 70°C and solution B was rapidly added under vigorous stirring until a precipitate was formed at pH = 4. Then, solution B was added slowly to avoid pH value of the mixture higher than 8. The mixture was heated during 2 h under stirring, then ripened at ambient temperature during 16 h. The precipitate was then filtered, washed with 1 L of deionized water then with ethanol (96 % vol.) and finally dried at 60 °C in an oven during 24 h. The yield of synthesis was determined from the analysis of Cu, Ca and P elemental concentrations remaining in the initial supernatant and in the washing solutions. This protocol allowed the synthesis of 4 mmol of Cu-Hap. No particular caution was paid to the carbonate content of $Ca(OH)_2$ solution.

2.2. Batch experiments

Batch experiments were performed at room temperature by contacting various Cu-Hap samples with several solutions contaminated with uranium in a Teflon container (Savillex). Synthetic solutions of 0.02 M $NaNO_3$ (Sigma Aldrich ReagentPlus) and Na_2SO_4 (Sigma Aldrich, ACS reagent) spiked with 1.0 mM of uranium nitrate homemade solution or real mining waters

were used. The pH of the synthetic spiked solution was adjusted using 8 M NaOH solution. The uranium concentration in the synthetic solution prepared was analyzed by Inductively Coupled Plasma – Atomic Emission Spectroscopy (ICP-AES) following the procedure described below. **Table 1** summarized the experimental conditions used in the various batch experiments.

Table 1. Experimental conditions for the batch experiments.

Cu content, x_{Cu}	Cu-Hap (mg)	Solution	Volume (mL)	C_U (initial) (mol/L)	pH (initial)
0.44/ 1.15/ 1.59	100	0.02 M Na_2SO_4	100	$(0.91 \pm 0.01) \times 10^{-3}$	7.1 ± 0.1
0.44/ 1.15/ 1.59	100	0.02 M $NaNO_3$	100	$(1.02 \pm 0.01) \times 10^{-3}$	7.2 ± 0.1
0.44/ 1.15/ 1.45/ 1.59	60	V105	200	$(0.97 \pm 0.04) \times 10^{-6}$	4.5 ± 0.1
0.44/ 1.15/ 1.45/ 1.59	60	BD200	200	$(1.64 \pm 0.02) \times 10^{-6}$	7.1 ± 0.1

The containers were placed in an orbital stirrer in order to ensure the homogeneity of the system. Regularly, pH were measured using a Metrohm combination-glass electrode calibrated against pH buffers (Inlab® Solutions, Mettler Toledo, pH =2.00; 4.01, 7.00 and 9.21 at 25°C) and 10 mL of solution were sampled to determine the elemental concentrations in U, Cu, Ca and P. The samples were first centrifuged at 4500 rpm during 10 min, then 9 mL of solution were taken off and acidified to pH ~ 2 with 0.5 mL of 0.2 M HNO_3 solution. The samples were analyzed either by ICP-AES (Spectro Arcos EOP device) or by ICP-MS (Thermo Scientific iCAP RQ). The calibration was performed using PlasmaCAL (SCP Science) single element calibration standards (C_U, C_{Ca}, C_{Cu} and C_P = 1000 ppm) diluted in HNO_3 solution. Concentrations and associated uncertainties were respectively the mean and twice the standard deviation of three replicates. This protocol allowed the detection as low as 50 ppb for Cu and 100

ppb for U, Ca and P. ICP-MS was used to measure lower concentrations using EN ISO 7980 and EN ISO 11885 standards for Ca, Cu and P analyses, respectively. NF M 60 805 4 standard was used to determine U elemental concentration.

The two mining waters (named V105 and BD200) were sampled at the former uranium mining site of Bellezane (Limousin, France). The composition of the two types of water was determined by ICP-AES calibrated against single element calibration standards (1000 ppm). The total inorganic carbon content was measured using a TOC analyzer (Shimadzu, Japan) after dilution of the mining water with 10 mL of deionized water. Total inorganic carbon concentration was measured using an external calibration curve prepared by dilution of a 500 ppm $NaHCO_3$ standard solution with deionized water. The detection limit reached 0.5 ppm of total carbon. The main characteristics of the two mining waters are reported in **Table 2**. The two samples differed mainly in terms of pH, sulfate, carbonate and elemental concentrations resulting from their different hydrogeological origin. Uranium concentrations $C_U = (1.60 \pm 0.02) \times 10^{-6}$ and $(0.97 \pm 0.04) \times 10^{-6}$ mol/L for BD200 and V105, respectively.

Table 2. pH, concentrations of main ions and inorganic carbon content determined by ICP-AES for the two mining waters collected in the Bellezane site. Simulations of uranium speciation in the two mining waters by Phreeqc Interactive[37] using Thermochimie[38, 39] and PRODATA[40] thermodynamic databases.

		BD 200	**V 105**
pH		7.1 ± 0.1	4.5 ± 0.1
Ca	**(mg/L)**	71.7 ± 0.2	149.1 ± 0.6
K	**(mg/L)**	8.0 ± 0.1	10.24 ± 0.1
Mg	**(mg/L)**	22.0 ± 0.2	64 ± 3
Na	**(mg/L)**	9.7 ± 0.4	12 ± 1
Al	**(mg/L)**	0.33 ± 0.01	30.1 ± 0.1
Cu	**(mg/L)**	< DL	< DL
U*	**(mg/L)**	0.38 ± 0.01	0.23 ± 0.01
S	**(mg/L)**	70 ± 2	225 ± 5
Si	**(mg/L)**	6.8 ± 0.2	20.2 ± 0.6
C*	**(mg/L)**	88.1 ± 0.2	4.36 ± 0.04

Main U(VI) species (%): Thermochimie TDB	
$Ca_2UO_2(CO_3)_3$: 67.7 %	$UO_2(SO_4)$: 62.6 %
$CaUO_2(CO_3)_3^{2-}$: 30.5 %	UO_2^{2+}: 24.1 %
$UO_2(CO_3)_2^{2-}$: 1.2 %	$UO_2SiO(OH)_3^{+}$: 6.1 %
	$UO_2(SO_4)_2^{2-}$: 3.8 %
	$UO_2(OH)^{+}$: 3.4 %
Main U(VI) species (%): PRODATA TDB[#]	
$Ca_2UO_2(CO_3)_3$: 67 %	$UO_2(SO_4)$: 60 %
$CaUO_2(CO_3)_3^{2-}$: 32 %	UO_2^{2+}: 27 %
	$UO_2SiO(OH)_3^{+}$: 6 %
	$UO_2(SO_4)_2^{2-}$: 3 %
	UO_2CO_3: 2 %
	UO_2OH^{+}: 2 %

*total inorganic carbon concentration analyzed by TOC meter. U analyzed by ICP-MS.
[#]data extracted from Reiller and Descostes[40]. PRODATA is a new thermodynamic database dedicated to mining and environmental monitoring activities.

2.3. Characterization of the solid phases

The stoichiometry of the prepared Cu-Hap was determined by complete dissolution of 30 mg of the solid in 30 mL of 0.2 M HNO_3. Four dilutions of the resulting solution with 0.2 M HNO_3 were performed then measured by ICP-AES analyses. Cu-Hap samples were characterized before and after being contacted with uranium solutions by Powder X-ray diffraction (PXRD), Raman spectroscopy, Time-Resolved Laser-induced Fluorescence Spectroscopy (TRLFS) and Scanning Electron Microscopy (SEM). PXRD patterns were recorded using a Bruker D8 advance diffractometer with copper radiation (λCu $K\alpha_{1,2}$ = 1.54184 Å) in a parallel mode and using the reflection geometry. The patterns were recorded between 5° and 100° (2θ) with a step of 0.02 ° and a counting time of 3 h. The resulting data were refined using the Fullprof_suite [41] by applying the Rietveld method and using the Thomson Cox profile function [42]. Pure silicon was used as a standard to determine instrumental parameters. Zero shift, unit cell parameters,

overall displacement, preferred orientation and anisotropic size model for the microstructural characteristics were considered for all the refinements.

Raman spectra were recorded by the means of a Horiba - Jobin Yvon Aramis apparatus equipped with an edge filter and using a Nd:YAG laser (532 nm). In order to avoid any laser-induced degradation of the compound, the power was turned down by the means of optical filters to about 1–4 mW depending on the sample analyzed. The laser beam was then focused on a small fraction of powder deposited on a glass lamella using an Olympus BX 41 microscope. A ×100 objective with a numerical aperture of 0.9 was used, resulting in a spot size of about 1 μm^2. The scattered Raman light was collected in a 180° backscattering geometry and dispersed by a grating of 1800 grooves/mm after having passed a 150 μm entrance slit, resulting in a spectral resolution lower than 1 cm^{-1}. For each spectrum, a dwell time of 90 to 180 s was considered with an average of 3 scans. Before analysis, the apparatus was calibrated with a silicon wafer, using the first-order Si line at 520.7 cm^{-1}.

TRLFS was performed with the experimental setup described in literature[43]. A Nd:YAG laser (266 nm, pulse duration 5 ns at 10 Hz) was used. In order to avoid laser ablation, the laser beam was driven through an optical system and a 50-μm diaphragm to reduce the beam diameter and the delivered energy. The beam was then focused close to the surface of the sample through a microscope lens (model BX-51). The surface of the sample was positioned near the focal plane of the laser to obtain a probed area of about 1 mm in diameter. TRLFS was performed on powder samples deposited on double-sided tapes. The fluorescence emission was collected by an optical fiber placed at 45° with respect to the axis of the laser and transmitted to a monochromator Andor Shamrock SR-303i (grating of 300 grooves/mm, entrance slit of 150 μm, spectral

resolution of about 15 nm). Each sample spectrum resulted from 300 accumulated spectra recorded with a temporal gate of 200 µs delayed by 1 µs after the laser pulse.

Scanning electron microscopy (SEM) analyses were conducted using a Quanta 200 ESEM FEG (FEI Company) electron microscope equipped either with a backscattered electron detector (BSED) in high vacuum conditions with a 25 kV accelerating voltage. Powder samples were directly analyzed without any preparation. Qualitative X-ray energy dispersive spectroscopy (X-EDS) analyses were performed under the same conditions using the Bruker AXS X-Flash 5010 detector coupled to the SEM device. X-EDS maps were obtained using the same detector and operating conditions. For that purpose, an aliquot of each sample was embedded in an epoxy resin, polished to optical grade and metalized by carbon deposition.

The specific surface area of the synthesized Cu-Hap powder were determined using 10 point adsorption isotherm of N_2(g) at 77 K and the B.E.T. method (Tristar, Micromeritics).

2.4. Speciation calculations

From the composition of the synthetic solutions or mining waters (**Table 2**), the average elemental concentrations and pH values of the systems at equilibrium, the saturation index of the solutions with respect to the solid phases of interest were calculated with the geochemical speciation model Phreeqc Interactive (Version 3.3.3)[37]. The solutions were considered at equilibrium with air (pO_2 = 0.2 atm and $pCO_2 = 10^{-3.5}$ atm). The calculations of the solubility product accounted for the aqueous complexation reactions incorporated in the Thermochimie database[38, 39]. The thermodynamic database was completed for Cu speciation using the data reported in the Minteq.V4 database[44] and for the standard solubility product of meta-autunite ($Ca(UO_2)_2(PO_4)_2 \cdot 3H_2O$), uranyl hydrogen phosphate ($UO_2HPO_4 \cdot 3H_2O$) and meta-torbernite

193 determined by Gorman-Lewis et al.[21] and by Cretaz et al.[22], respectively. The activity
194 coefficients were calculated using the Davies equation implemented in the Phreeqc software.
195

196 ## 3. RESULTS AND DISCUSSION

197 ### 3.1.Characterizations of prepared Cu-Hap

198 The composition of the prepared Cu-Hap is indicated in **Table 3**. The Cu mole fraction
199 determined by total dissolution of the sample differed slightly from the expected value and
200 showed a decrease of the Ca incorporation yield when increasing the Cu content in the starting
201 mixture. This decrease led to the formation of non-stoichiometric Cu-Hap (with $\frac{x_{Cu}+x_{Ca}}{x_P} \neq 1.67$).
202 The PXRD patterns of the synthesized Cu-Hap is presented in **Figure 1**. All patterns showed the
203 XRD lines related to the hexagonal structure of hydroxyapatite (space group $P6_3/m$), excluding
204 the presence of secondary phase. The prepared samples were thus single phase for $x_{Cu} \leq 1.59$.
205 The Rietveld refinement of the patterns indicated the contraction of the unit cell volume versus
206 the incorporation rate of copper (**Table 3**), as the result of the replacement of calcium by the
207 smaller copper in the structure. The unit-cell volume of the prepared Cu-Hap were also
208 compared to several values reported in the literature (**Figure S2** included in the supporting
209 information). The results agreed well with the data reported by Shanmugam et al.[30] and Li et al.[32]
210 for Cu substituted Hap. The unit cell volume presented a minimum for $x_{Cu} = 0.44$ (i.e. V =
211 524.86(8) $Å^3$), then was found to be almost constant for $x_{Cu} = 1.15$; 1.45 and 1.59. Shanmugam
212 et al.[30] obtained smaller unit cell volumes for $0.05 \leq x_{Cu} \leq 0.25$ then observed an increase for x_{Cu}
213 = 0.5 (i.e. V= 525.6 $Å^3$), which is in agreement with the data determined for $x_{Cu} = 0.44$. Such a
214 variation of the unit cell volume when substituting Ca by Cu could indicate different
215 incorporation modes in the solid solution, i.e. substitution in Ca1 or Ca2 sites and/or insertion in

the structure. Similar behavior was observed by Gomes et al.[45] for Zn-Hap in which Zn atoms occupy interstitial sites in Hap (Wyckoff site 2*b*), leading to solid solution with general composition $Ca_{10}Zn_x(PO_4)_6O_{2x}(OH)_{2-2x}$. Even if different substitution/incorporation mechanisms could have led to the precipitation of these Cu-Hap samples, the variation of the unit cell volume versus the copper content indicates that copper was not only adsorbed at the surface of Hap, but incorporated in the lattice. This result suggests that the rate of Cu release in solution may be controlled by the dissolution of the Cu-Hap sample.

Table 3. Reaction yield of precipitation determined from the analysis of the supernatant by ICP-AES. Copper mole fraction x_{Cu} and $(x_{Cu}+x_{Ca})/x_P$ ratio determined by total dissolution of the precipitate, unit cell parameters determined by Rietveld refinement from PXRD patterns and specific surface area of the synthesized Cu-Hap. The copper contents in the Cu-Hap taken from the literature corresponds to the stoichiometry of the mixture of reactants during the synthesis (except for Stanić et al.[34]).

Ca yield (mol. %)	**Cu yield (mol. %)**	**P yield (mol. %)**	$\mathbf{x_{Cu}}$	$\frac{x_{Cu}+x_{Ca}}{x_P}$	**a (Å)**	**c (Å)**	**Cell volume (Å^3)**	$\mathbf{S_{BET}}$ **(m²/g)**
99.9 ± 0.1	N.D.	99.9 ± 0.1	0	1.7 ± 0.1	9.4213(3)	6.8908(2)	529.69(2)	80
97.6 ± 0.1	99.9 ± 0.1	99.8 ± 0.1	0.44 ± 0.01	1.9 ± 0.2	9.3859(8)	6.8794(6)	524.86(8)	85
88.5 ± 0.3	98.9 ± 0.1	95.6 ± 0.1	1.15 ± 0.01	1.4 ± 0.2	9.4240(5)	6.8500(4)	526.87(5)	147
82.9± 0.2	99.2 ± 0.1	96.0± 0.3	1.45 ± 0.01	1.5 ± 0.2	9.4282(6)	6.8493(4)	527.28(5)	76
N.D.	N.D.	N.D.	1.59 ± 0.01	1.6 ± 0.2	9.404(1)	6.8728(8)	526.4(1)	65
Shanmugam et al.[30]			0		9.42	6.88	528.8	
			0.05		9.328(4)	6.844(3)	515.6	
			0.1		9.358(9)	6.837(9)	518.7	
			0.15		9.333(0)	6.843(3)	516.2	
			0.2		9.353(2)	6.842(7)	518.4	
			0.25		9.337(8)	6.842(7)	516.7	
			0.5		9.397(0)	6.872(7)	525.6	
Karpov et al.[46]			0.54		9.4303(1)	6.9069(1)	531.95(1)	
Stanić et al.[34]			0	1.65	9.4261	6.8971	530.71	
			0.0042	1.65	9.4249	6.8957	530.40	
			0.041	1.63	9.4218	6.8954	530.10	

N.D.: not determined

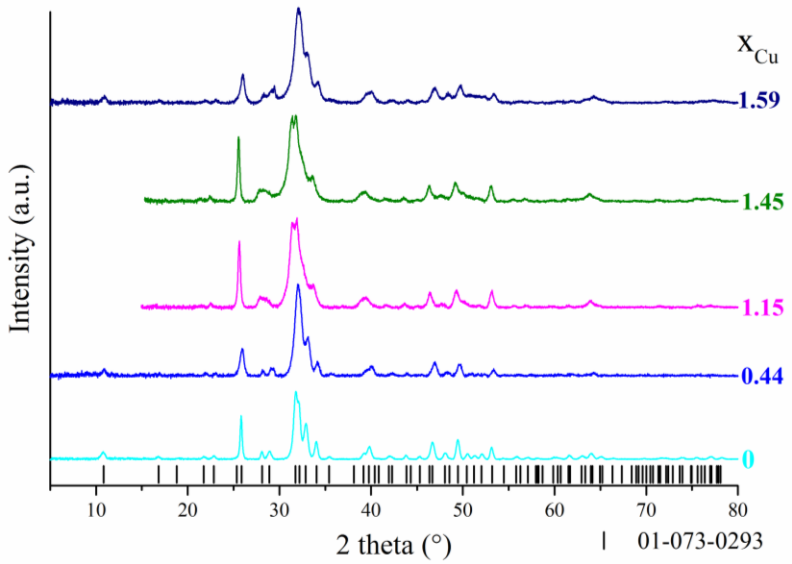

Figure 1. PXRD patterns of the synthesized Cu-Hap. Black bars are the Bragg positions for stoichiometric Hap (PDF 01-073-0293).

The Raman spectra recorded for all the synthesized Cu-Hap are showed in **Figure 2** as well as the position of the bands obtained for $x_{Cu} = 0$. The strongest Raman active mode ν_1[45, 47, 48] associated to symmetric stretching of the P-O bond was observed at 963 cm^{-1} and did not shift when increasing the Cu content. As an example, O'Donnell et al.[48] showed that the position of the ν_1 band decreased linearly from 963 cm^{-1} (Hap) to 949 cm^{-1} for full substitution of Ca by heavier Sr. For Zn-substituted Hap, Gomes et al.[45] observed that the intense single band at 963 cm^{-1} was split in three resolved contributions indicating a local structure ordering. The absence of shift in energy of this mode for the Cu-substituted hydroxyapatite indicates a negligible compositional effect. The variation of the peak intensity was not correlated to the Cu content, but rather revealed different degrees of crystallinity of the samples.

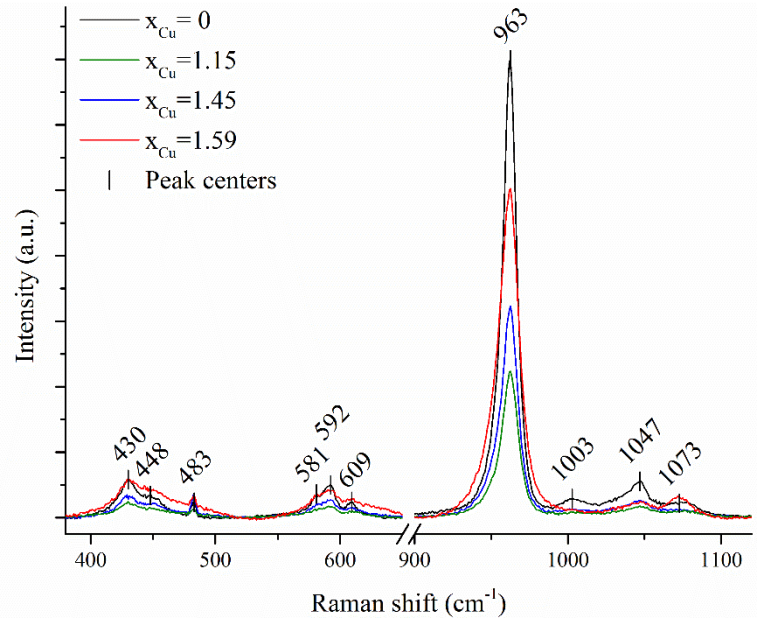

Figure 2. Raman spectra of the synthesized Cu-Hap.

3.2. Batch experiments

The prepared Cu-Hap were put in contact with solutions spiked with uranium. The composition of the solutions at equilibrium with the Cu-Hap is listed in **Table 4**. The evolution of the uranium concentration in the two mining waters contacted with the different Cu-Hap samples is reported in **Figure 3**. The evolution of phosphorus and copper concentrations in BD200 and V105 mining waters are showed in **Figure S3** and **Figure S4** of supporting information, respectively.

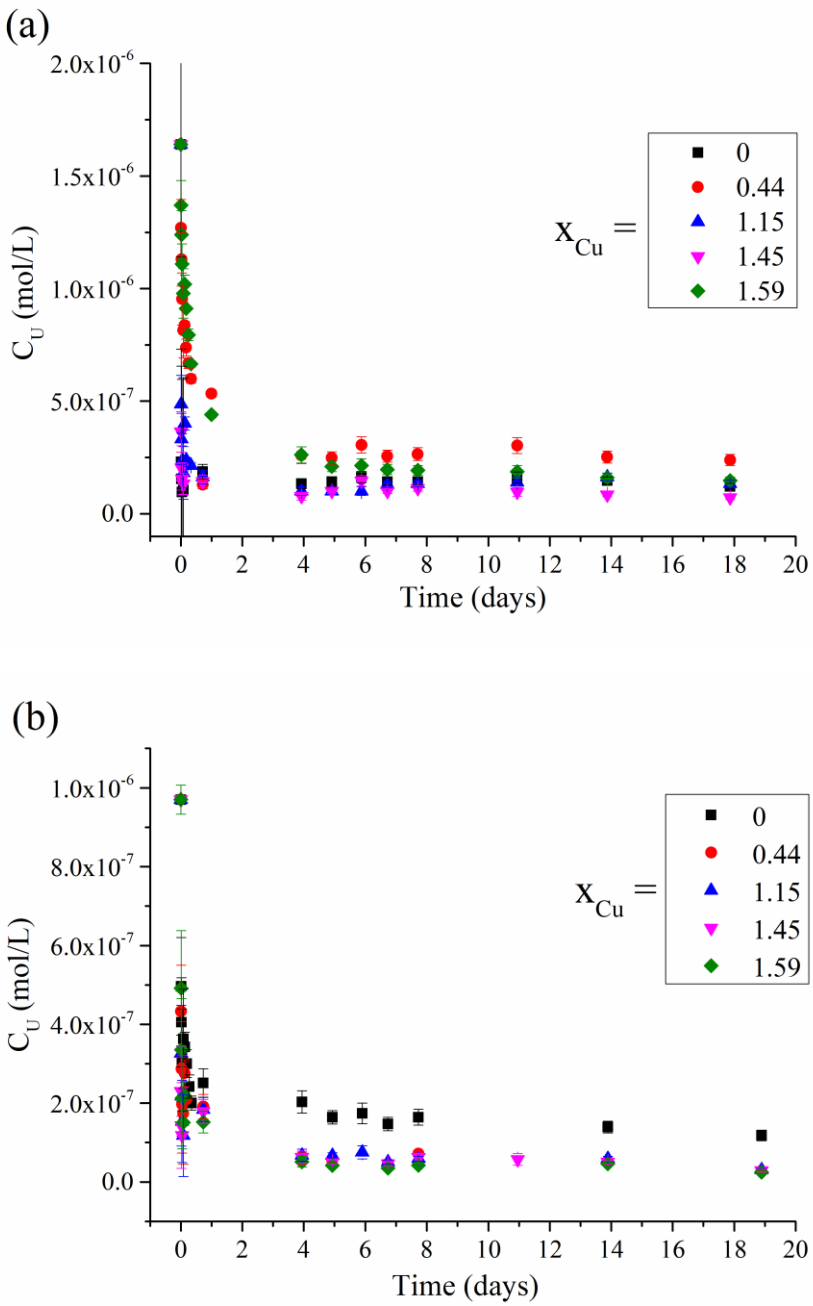

Figure 3. Evolution of the U elemental concentrations in BD200 (a) and V105 (b) mining waters when contacting with the different prepared Cu-Hap samples.

From these results, a fast decrease of the uranium concentration was observed, followed by the establishment of an equilibrium after 4 days of contact with the mining waters. For experiments involving BD200 mining water, uranium concentrations obtained at equilibrium

with the Cu-Hap were found to vary between 0.7 $\times 10^{-7}$ to 2.4 $\times 10^{-7}$ mol/L without any correlation with the amount of Cu incorporated in the Cu-Hap. For V105 mining water, it ranged between 0.2 $\times 10^{-7}$ to 1.2 $\times 10^{-7}$ mol/L and slightly decreased with increase of the Cu mole fraction in Cu-Hap. The benefit linked to the increase of the Cu content in the hydroxyapatite structure was only significant for V105 mining water. V105 is more acidic than BD200 and the synthetic solutions and contains less carbonate ions and more sulfate ions, affecting the speciation of uranium in the mine waters (**Table 2**). $Ca_2(UO_2)(CO_3)_3$ and $CaUO_2(CO_3)_3^{2-}$ were found to be the predominant species in BD200 (68 and 31%, respectively) whereas $UO_2(SO_4)$ and free UO_2^{2+} were predominant in V105 (63 and 24%, respectively).

The results obtained for the 0.02 mol/L $NaNO_3$ and Na_2SO_4 synthetic solutions spiked with 10^{-3} mol/L of uranium are given in supporting information (**Figure S5** and **Figure S6**, respectively). Once again, a strong and fast decrease of the uranium elemental concentration was observed. Uranium concentration obtained at equilibrium with Cu-Hap varied from 0.5 $\times 10^{-6}$ to 2 $\times 10^{-6}$ mol/L whatever the Cu content in the Hap sample and the composition of the solution. This decrease reached 3 orders of magnitude after only 1 day, showing that the presence of sulfate or nitrate ions did not affect significantly the apparent solubility of the neoformed phase. This result was supported by speciation calculations, which showed similar distribution of uranium in all the synthetic solutions. Indeed, $(UO_2)_2CO_3(OH)_3^-$ was the predominant species in both 0.02 M $NaNO_3$ and Na_2SO_4 solutions (87.5 and 93.4%, respectively).

Table 4. Composition of the synthetic solutions at equilibrium with the Hap-Cu with various Cu contents. Calculated saturation index of the solutions relative to meta-torbernite (S.I. MT) and autunite (S.I. AU) using Phreeqc associated to selected thermodynamic data[21, 22, 38, 39, 44].

x_{Cu}	C_U (initial) (mol/L)	pH eq	C_U eq (mol/L)	C_{Cu} eq (mol/L)	C_P eq (mol/L)	C_{Ca} eq (mol/L)	S.I. (MT)	S.I. (AU)
				0.02 M Na_2SO_4				
0	$(0.91 \pm 0.01)\times10^{-3}$	7.1 ± 0.1	$(0.7 \pm 0.2)\times10^{-6}$	< D.L.	$(6.9 \pm 0.8)\times10^{-6}$	$(1.10 \pm 0.02)\times10^{-3}$	N.D.	3.21
0.44	$(0.91 \pm 0.01)\times10^{-3}$	7.1 ± 0.1	$(2.1 \pm 0.8)\times10^{-6}$	$(1.3 \pm 0.2)\times10^{-6}$	$(7.3 \pm 0.5)\times10^{-6}$	$(1.13 \pm 0.02)\times10^{-3}$	3.31	3.39
1.15	$(0.91 \pm 0.01)\times10^{-3}$	7.1 ± 0.1	$(0.9 \pm 0.2)\times10^{-6}$	$(1.7 \pm 0.5)\times10^{-6}$	$(13.9 \pm 0.3)\times10^{-6}$	$(1.16 \pm 0.02)\times10^{-3}$	3.79	3.75
1.59	$(0.91 \pm 0.01)\times10^{-3}$	7.1 ± 0.1	$(0.5 \pm 0.3)\times10^{-6}$	$(1.5 \pm 0.5)\times10^{-6}$	$(12.3 \pm 0.7)\times10^{-6}$	$(1.14 \pm 0.01)\times10^{-3}$	3.04	3.11
				0.02 M $NaNO_3$				
0	$(1.02\pm 0.01)\times10^{-3}$	7.2 ± 0.1	$(1.6 \pm 0.9)\times10^{-6}$	< D.L.	$(9 \pm 1)\times10^{-6}$	$(1.26 \pm 0.04)\times10^{-3}$	N.D.	5.04
0.44	$(1.02\pm 0.01)\times10^{-3}$	7.2 ± 0.1	$(1.8 \pm 0.4)\times10^{-6}$	$(1.5 \pm 0.2)\times10^{-6}$	$(6.5 \pm 0.2)\times10^{-6}$	$(1.19 \pm 0.02)\times10^{-3}$	4.20	4.21
1.15	$(1.02\pm 0.01)\times10^{-3}$	7.2 ± 0.1	$(1.5 \pm 0.8)\times10^{-6}$	$(1.5 \pm 0.4)\times10^{-6}$	$(15 \pm 1)\times10^{-6}$	$(1.23 \pm 0.01)\times10^{-3}$	5.20	5.12
1.59	$(1.02\pm 0.01)\times10^{-3}$	7.2 ± 0.1	$(1.0 \pm 0.6)\times10^{-6}$	$(1.0 \pm 0.3)\times10^{-6}$	$(10 \pm 1)\times10^{-6}$	$(1.23 \pm 0.01)\times10^{-3}$	4.72	4.74
				V105				
0	$(0.97 \pm 0.04)\times10^{-6}$	4.2 ± 0.1	$(1.2 \pm 0.1)\times10^{-7}$	< D.L.	$(4.7 \pm 0.4)\times10^{-5}$	$(3.8 \pm 0.6)\times10^{-3}$	N.D.	-1.30
0.44	$(0.97 \pm 0.04)\times10^{-6}$	5.1 ± 0.1	$(0.28 \pm 0.03)\times10^{-7}$	$(1.87\pm 0.04)\times10^{-4}$	$(1.1 \pm 0.1)\times10^{-5}$	$(4.0 \pm 0.6)\times10^{-3}$	1.49	-0.50
1.15	$(0.97 \pm 0.04)\times10^{-6}$	4.5 ± 0.1	$(0.31 \pm 0.03)\times10^{-7}$	$(1.70\pm 0.04)\times10^{-4}$	$(4.0 \pm 0.3)\times10^{-5}$	$(3.9 \pm 0.6)\times10^{-3}$	0.74	-1.47
1.45	$(0.97 \pm 0.04)\times10^{-6}$	4.6 ± 0.1	$(0.29 \pm 0.04)\times10^{-7}$	$(2.20\pm 0.03)\times10^{-4}$	$(4.0 \pm 0.3)\times10^{-5}$	$(3.9 \pm 0.6)\times10^{-3}$	1.03	-1.23
1.59	$(0.97 \pm 0.04)\times10^{-6}$	4.8 ± 0.1	$(0.25 \pm 0.03)\times10^{-7}$	$(1.69\pm 0.08)\times10^{-4}$	$(5.8 \pm 0.4)\times10^{-5}$	$(4.1 \pm 0.6)\times10^{-3}$	1.65	-0.42
				BD200				
0	$(1.64 \pm 0.02)\times10^{-6}$	7.6 ± 0.1	$(1.2 \pm 0.1)\times10^{-7}$	< D.L.	$(4 \pm 1)\times10^{-6}$	$(1.49 \pm 0.02)\times10^{-3}$	N.D.	-0.98
0.44	$(1.64 \pm 0.02)\times10^{-6}$	7.7 ± 0.1	$(2.4 \pm 0.2)\times10^{-7}$	$(1.1 \pm 0.1)\times10^{-6}$	$(2.6 \pm 0.8)\times10^{-6}$	$(1.63 \pm 0.02)\times10^{-3}$	-2.07	-1.16
1.15	$(1.64 \pm 0.02)\times10^{-6}$	7.7 ± 0.1	$(1.3 \pm 0.2)\times10^{-7}$	$(1.3 \pm 0.2)\times10^{-6}$	$(5 \pm 1)\times10^{-6}$	$(1.55 \pm 0.03)\times10^{-3}$	-1.61	-0.81
1.45	$(1.64 \pm 0.02)\times10^{-6}$	7.7 ± 0.1	$(0.7 \pm 0.1)\times10^{-7}$	$(1.4 \pm 0.1)\times10^{-6}$	$(11 \pm 1)\times10^{-6}$	$(1.58 \pm 0.02)\times10^{-3}$	-1.50	-0.70
1.59	$(1.64 \pm 0.02)\times10^{-6}$	7.7 ± 0.1	$(1.5 \pm 0.2)\times10^{-7}$	$(0.69 \pm 0.06)\times10^{-6}$	$(5 \pm 1)\times10^{-6}$	$(1.59 \pm 0.03)\times10^{-3}$	-2.00	-1.03

U concentrations at equilibrium with BD200 and V105 measured by ICP-MS for BD200 and V105 and by ICP-AES for the other solutions. The uncertainties associated to the concentrations at equilibrium were estimated as the standard deviation between consecutive concentrations values that were not significantly different considering the experimental errors. < D.L.: below detection limit. N.D.: not determined.

In order to gain insights in the mechanism associated to the uranium uptake by Cu-Hap, the saturation indices (S.I.) with respect to uranium containing phases were calculated using the final concentrations and pH for the various experiments (pH eq and C_i eq, **Table 4**) and the Phreeqc software associated to selected thermodynamic data[21, 22, 38, 39, 44]. Positive S.I. values indicate that

293 the bulk solution is oversaturated with respect to the phase of interest, thus that precipitation of
294 the phase may occur.

295 For near neutral pH values, the synthetic solutions were found to be highly oversaturated
296 with respect to meta-autunite and meta-torbernite. The calculated S.I. of these two phases were
297 very close and did not allow to conclude which precipitation is privileged in the bulk solution. At
298 the end of these experiments, it is worth noting that the synthetic solutions were close to
299 equilibrium or slightly oversaturated with respect to hydroxyapatite[49] (S.I. (Hap) varying from -
300 0.35 to 2.17).

301 For BD200 mining water (pH eq = 7.7), the S.I. with respect to meta-torbernite and
302 autunite were negative, which indicated that precipitation in the bulk solution was not the driving
303 mechanism for uranium removal from solution. At the end of the experiments performed in
304 BD200, the solutions remained highly oversaturated with respect to hydroxyapatite, with S.I.
305 ranging from 4.7 to 6.5. The fact that the Cu-Hap was not dissolved in BD200 also argued in
306 favor of adsorption or surface precipitation caused by local saturation as the most likely
307 mechanisms.

308 For V105 mining water (pH eq < 5), meta-torbernite was the only uranium bearing phase
309 with positive S.I. at the end of experiments. Also, the solutions remained highly undersaturated
310 with respect to hydroxyapatite with S.I. ranging from -12.4 to -7.9. In such acidic solution, Cu-
311 Hap was dissolved whereas meta-torbernite was precipitated in the bulk solution, leading to the
312 immobilization of uranium.

313 **3.3. Characterization of neoformed phases**

314 At the end of the batch experiments, solid and liquid phases were separated by
315 centrifugation and the solid phase was characterized systematically by PXRD. As an example,

316 the patterns recorded for the Cu-Hap with x_{Cu} = 1.59 contacted with the sodium nitrate and
317 sodium sulfate solutions spiked with uranyl are presented in **Figure 4**. The PXRD patterns
318 recorded for the Cu-Hap sample contacted with the synthetic solutions presented characteristic
319 peaks of a mixture of Hap and chernikovite (for $x_{Cu} = 0$) or meta-torbernite (for $x_{Cu} > 0$). These
320 patterns were refined by the Rietveld method to quantify the weight fraction of uranium bearing
321 phase in the mixture of crystalline phases (**Table 5**). All the samples exposed to the synthetic
322 solutions spiked with uranium at 10^{-3} mol/L presented high weight fraction of uranium (from 24
323 to 29 wt. %). The uranium loading calculated from the refinement of the PXRD patterns of the
324 remaining solid phase was found to be lower or close to the uranium weight fraction calculated
325 from the decrease of the uranium concentration in solution. This result indicated that a major part
326 of uranium (from 55 to 100 %) was uptaken from the solution by precipitation in a crystalline
327 phase. For Cu-undoped Hap structure, the neoformed phase was chernikovite (also called H-
328 autunite). It was also observed in the uranium phase precipitates by Fanizza et al.[3], Lammers et
329 al.[14]. and Fuller et al.[5]. Simon et al.[12] reported the formation of chernikovite in mixtures with
330 autunite and meta-autunite. Mehta et al.[6] also reported its formation in the absence of Ca or Na
331 co-solutes. Lingjun Kong et al.[16], as well as Minhua Su et al.[17] observed the incorporation of
332 U(VI) ions into autunite after removal from mining water by biochar Hap and porous Hap,
333 respectively. It is noteworthy that meta-autunite is the thermodynamically stable phase in our
334 conditions, but the formation of chernikovite is reported to be kinetically favored[6, 12, 50]. Fuller et
335 al.[5] determined a threshold for the onset of chernikovite formation. Below 0.58 ± 0.08 wt. % of
336 uranium loading (i.e. 0.44 µmol/m² of uranium at the surface of Hap), the mechanism of sorption
337 is dominated by surface complexation. Above this limit, nucleation of chernikovite occurs either
338 at the Hap surface or in the bulk solution. Finally, depending on the composition of solution and

time, chernikovite can be transformed to meta-autunite by cationic exchange. For the synthetic spiked solutions, U loadings of the Hap were much higher than the threshold authorizing precipitation of chernikovite. Immobilization of uranium contacted with the Cu-Hap could have followed a similar sorption mechanism. However, due to the presence of copper, meta-torbernite was the uranium solubility controlling phase.

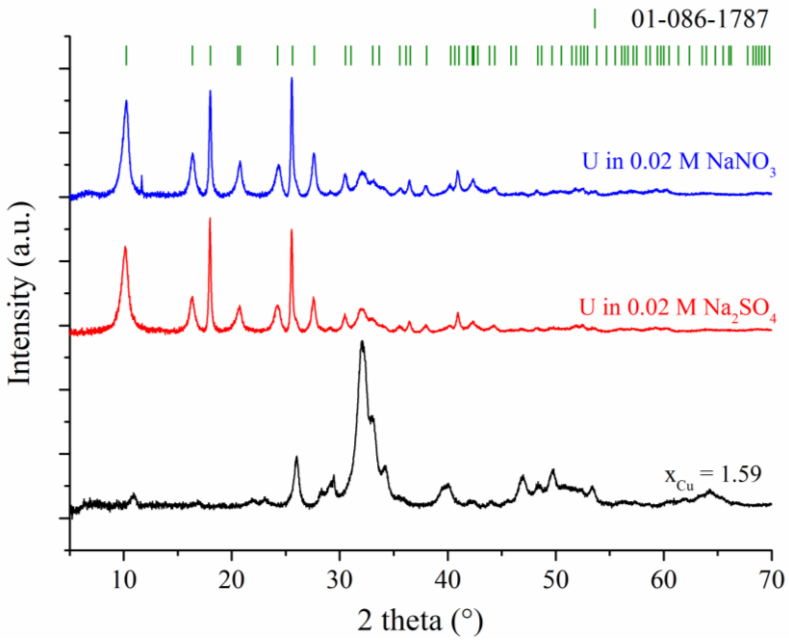

Figure 4. PXRD patterns of Cu-Hap sample (x_{Cu} = 1.59) before (black line) and after contact with 0.02 M Na_2SO_4 (red line) and $NaNO_3$ (blue line) solutions doped with uranium (~10^{-3} mol/L). The green bars correspond the Bragg positions obtained for meta-torbernite (PDF 01-086-1787).

The PXRD patterns recorded for Cu-Hap samples contacted with V105 and BD200 mining waters are gathered in the supporting information (**Figure S4**). The PXRD patterns recorded at the end of the batch experiments were similar to the XRD diagram of the starting Cu-Hap. Considering the low amount of U immobilized in the solid phase (**Table 5**), the weight fraction of any precipitated crystalline phase would be too low to be identified by PXRD, except for the sample corresponding to x_{Cu} = 1.45 and contacted with V105. Raman spectroscopy was used to

355 characterize the solid phase at the end of the batch experiments. In order to illustrate the results,
356 Raman spectra obtained for Cu-Hap samples (x_{Cu} = 1.45) contacted with V105 and BD200
357 mining waters are compared to the Raman spectrum of the synthetic meta-torbernite (**Figure S5**).
358 This comparison did not show the presence of the characteristic bands of meta-torbernite.
359 Especially, the very intense band ascribed to the symmetric stretching vibration of UO_2^{2+} at 826
360 cm^{-1} [51] was not observed in the Raman spectra of Cu-Hap samples contacted with mining waters.
361 These techniques are not sensitive enough to give insights into the mechanism of uranium
362 removal from the mining waters.
363

Table 5. Uranium loading of the solid phase calculated from C_U decrease in solution at equilibrium (by m², mol or mass of Cu-Hap introduced in the batch experiment) and calculated from Rietveld refinement of the PXRD patterns of the solid phase after exposure to spiked synthetic solutions ($C_U \sim 10^{-3}$ mol/L) and mining waters ($C_U \sim 10^{-6}$ mol/L). Summary of SEM observations of the samples.

	From U analysis in solution			From solid phase characterizations			
x_{Cu}	U loading µmoles/m²	U loading mol. %	U loading wt. %	U-phase wt. % XRD	Phase identified by XRD	U loading wt. % XRD	SEM
				0.02 M Na_2SO_4			
0	12.8 ± 0.1	103 ± 1	24 ± 1	32 ± 1	$H_3O(UO_2)(PO_4)\cdot 3H_2O$	20 ± 1	TP
0.44	12.1 ± 0.1	105 ± 1	25 ± 1	24 ± 2	$Cu(UO_2)_2(PO_4)_2\cdot 8H_2O$	14 ± 1	TP
1.15	7.2 ± 0.1	108 ± 1	25 ± 1	30 ± 1	$Cu(UO_2)_2(PO_4)_2\cdot 8H_2O$	18 ± 1	TP
1.59	16.3 ± 0.1	110 ± 1	25 ± 1	54 ± 1	$Cu(UO_2)_2(PO_4)_2\cdot 8H_2O$	32 ± 1	TP+s
				0.02 M $NaNO_3$			
0	14.6 ± 0.1	117 ± 1	28 ± 1	29 ± 1	$H_3O(UO_2)(PO_4)\cdot 3H_2O$	18 ± 1	TP
0.44	13.7 ± 0.1	118 ± 1	28 ± 1	22 ± 1	$Cu(UO_2)_2(PO_4)_2\cdot 8H_2O$	13 ± 1	TP
1.15	8.1 ± 0.1	123 ± 1	28 ± 1	40 ± 1	$Cu(UO_2)_2(PO_4)_2\cdot 8H_2O$	24 ± 1	TP
1.59	18.5 ± 0.1	125 ± 1	29 ± 1	45 ± 1	$Cu(UO_2)_2(PO_4)_2\cdot 8H_2O$	27 ± 1	TP
				BD200*			
0	0.07 ± 0.01	0.6	0.13	< D.L.			TP
0.44	0.06 ± 0.01	0.5	0.12	< D.L.			TP
1.15	0.04 ± 0.01	0.6	0.13	< D.L.			TP
1.45	0.08 ± 0.01	0.6	0.14	< D.L.			TP+s
1.59	0.08 ± 0.01	0.6	0.13	< D.L.			TP
				V105*			
0	0.04 ± 0.01	0.3	0.07	< D.L.			s
0.44	0.04 ± 0.01	0.3	0.07	< D.L.			S
1.15	0.02 ± 0.01	0.3	0.07	< D.L.			S
1.45	0.04 ± 0.01	0.3	0.07	2 ± 1	$Cu(UO_2)_2(PO_4)_2\cdot 8H_2O$	1.2 ± 1	S
1.59	0.05 ± 0.01	0.3	0.07	< D.L.			S

< D.L.: below detection limit. $H_3O(UO_2)(PO_4)\cdot 3H_2O$: chernikovite (PDF 01-075-1106); $Cu(UO_2)_2(PO_4)_2\cdot 8H_2O$: meta-torbernite (PDF 01-086-1787).

*Analyses of uranium concentrations at equilibrium performed by ICP-MS. TP: thin platelets covering Cu-Hap observed by SEM, s: presence of small square-shaped crystals (less than 1×1 µm²) observed by SEM, S: presence of large square-shaped crystals (more than 3×3 µm²) observed by SEM.

In order to confirm the precipitation of uranium from the synthetic doped solutions either as chernikovite (for $x_{Cu} = 0$), or as meta-torbernite (for $x_{Cu} > 0$), SEM micrographs were recorded in the backscattered electron mode. The micrographs presented in **Figure 5** showed the presence of Cu-Hap agglomerates covered by thin platelets showing a strong backscattered emission indicative of uranium. X-EDS maps (supporting information, **Figure S6**) evidenced the precipitation of uranium as secondary phase at the surface of Cu-Hap, which confirms the uranium uptake from the synthetic solutions spiked with $C_U \sim 10^{-3}$ mol/L. Additionally, the presence of bright platy squared-shape crystals of 0.5×0.5 µm² in size was identified for Cu-Hap contacted with synthetic sulfate solution ($x_{Cu} = 1.59$, see $x_{Cu} = 1.59$/ S in **Figure 5**). This morphology was characteristic of crystals of the autunite family[5, 16, 19, 22, 52].

For Cu-Hap samples contacted with the BD200 mining water, U was not detected by X-EDS. However, backscattered images showed the presence of thin platelets covering the surface of agglomerates of Cu-Hap particles (**Figure 6**). In the samples contacted with V105, the presence of bright and platy squared-shape crystals was systematically observed (**Figure 6**). The crystals reached 2 to 4 µm in size for Cu-Hap compared to 0.5 µm for non-substituted Hap ($x_{Cu} = 0$). U, P, Ca, Cu and Al were detected by X-EDS in the squared-shape grains. Although the quantification of the mass content of each element in the square-shaped crystals was difficult due to the vicinity of Cu-Hap particles, U elemental content was found to vary between 40 wt.% (for $x_{Cu} = 0$) and 62 wt. % for ($x_{Cu} = 1.59$), which was consistent with the precipitation of either chernikovite, autunite or meta-torbernite phases.

The different morphologies of uranium bearing phase observed for the samples contacted with V105 and BD200 mining waters could indicate the existence of different immobilization mechanisms for uranium. This assumption was strengthened by the values of saturation index

398 calculated for the bulk solution (**Table 4**). Indeed, positive saturation indexes was found for
399 meta-torbernite at the end of experiments for Cu-Hap contacted with V105, whereas negative
400 saturation indexes were determined for meta-torbenite and autunite for Cu-Hap contacted with
401 BD200. The main reason for this discrepancy was due to differences of the pH value, which was
402 much lower for V105 than for BD200. During the experiments with V105, such pH favored the
403 dissolution of the Cu-Hap and finally led to the strong increase of the Ca, Cu and P
404 concentrations in the solution. This allowed the establishment of oversaturated conditions in the
405 bulk solution with respect to meta-torbernite even for low uranium concentration in solution. On
406 the contrary, for experiments with BD200, the formation of thin platelet crystals could result
407 from local oversaturation when U, P, Ca and/or Cu concentrations were higher at the Cu-Hap
408 surface than in the bulk. A similar mechanism was evidenced by Ohnuki et al.[28]. It was called
409 surface mineralization. Nevertheless, the presence of brighter thin platelets could also result from
410 uranium sorption phenomena onto the surface of Cu-Hap, as already evidenced by Fuller et al.[5]
411 for Hap using low uranium loadings.

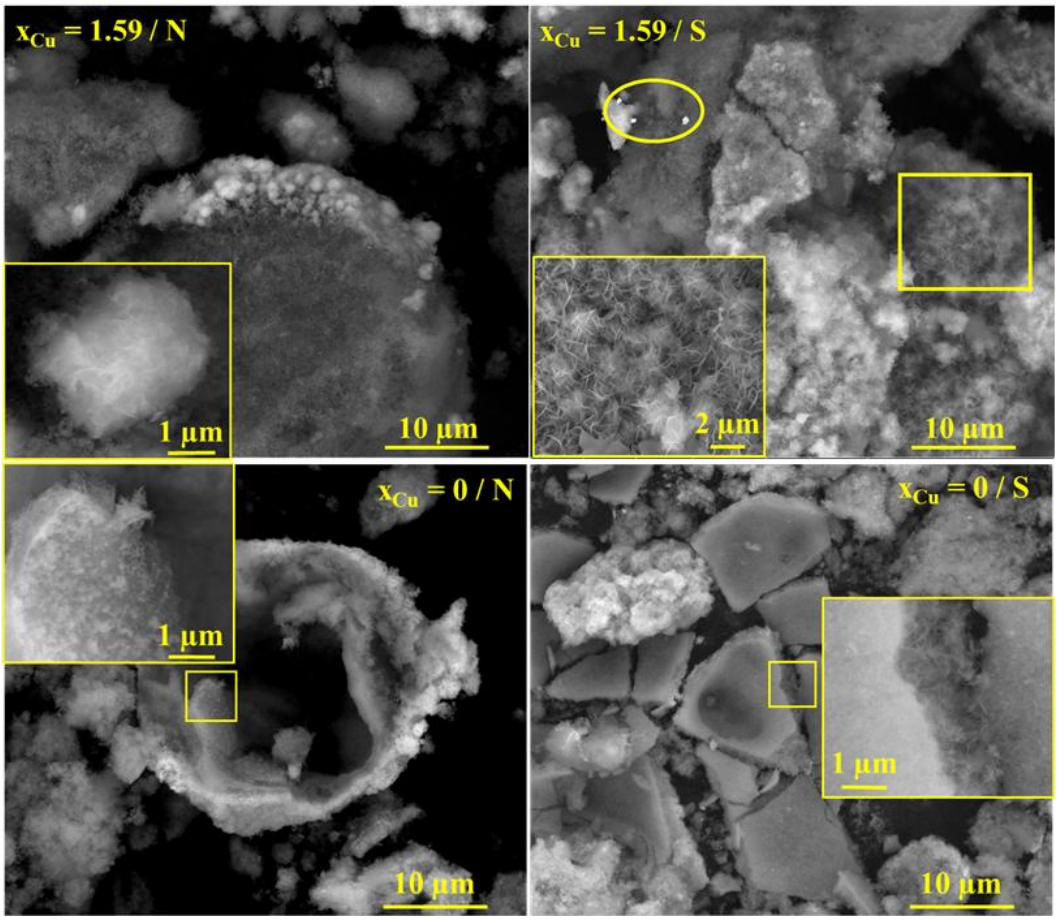

412

413 **Figure 5.** SEM micrographs (backscattered electron mode) of Cu-Hap resulting from the
414 contact with synthetic solutions doped with uranyl (C_U ~ 10^{-3} mol/L), showing the
415 presence of very thin platelets covering the Cu-Hap surfaces (bright areas). The
416 yellow-circled zone highlights the presence of square-shaped uranium bearing
417 crystals.

418

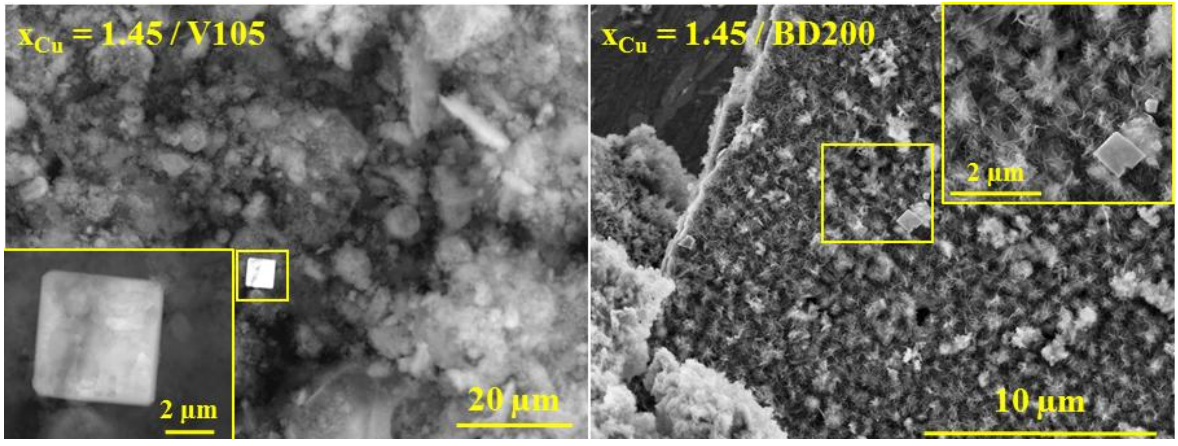

419

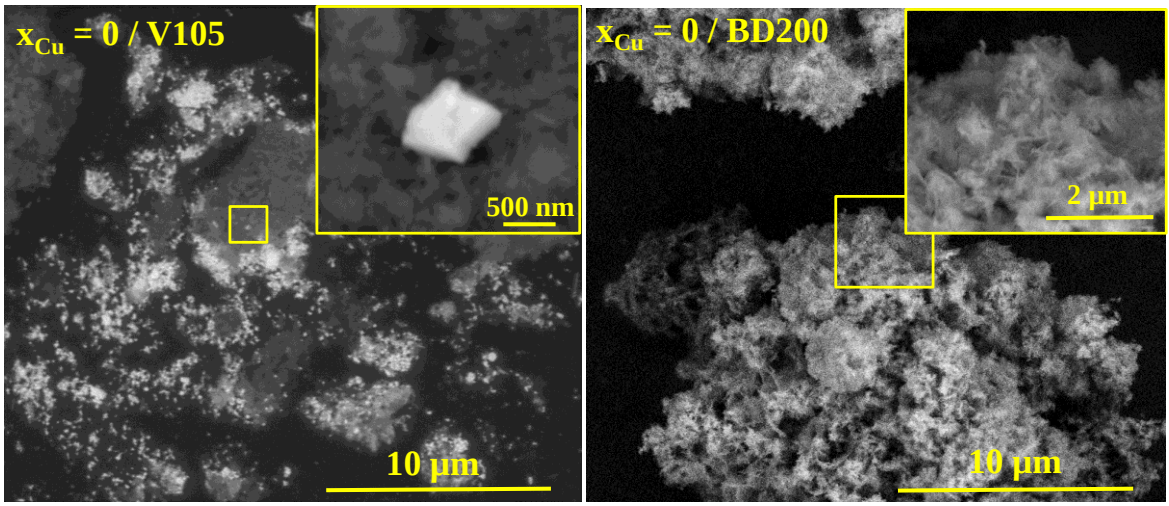

Figure 6. SEM micrographs of Cu-Hap (x_{Cu} = 1.45) resulting from contact with mining waters V105 and BD200 (backscattered electron mode, except for x= 1.45/ BD200) containing uranyl ($C_U \sim 10^{-6}$ mol/L). The images at high magnifications highlights the presence of square-shaped uranium bearing crystals of various sizes.

The TRLFS spectra of Cu-Hap samples at the end of the batch experiments are reported in **Figure 7**. All the spectra were characteristic of the luminescence of U(VI) compounds, with the observation of the five main peaks in the 480-600 nm range. The fluorescence spectra of the samples contacted with the synthetic solutions of uranyl in Na_2SO_4 (**Figure 7 a**) or $NaNO_3$ (**Figure 7 b**) synthetic solutions were all similar whatever the Cu content. These spectra were also comparable, in terms of peak locations, to the spectra recorded for synthesized meta-autunite, meta-torbernite and chernikovite (peaks positions and FWHM are gathered in **Table S1** of the supporting information). The larger peak widths in the sample spectra probably suggested a lower degree of crystallinity or different crystal shapes. TRLFS hardly distinguished meta-torbernite from chernikovite, which appears in agreement with previous recordings on chernikovite[53] and meta-torbernite minerals[54]. It can be inferred that the luminescence of U(VI) in both minerals is similar due to the very similar local environment of uranyl in both

438 structures[55-57]. As a matter of fact, regardless of the Cu content in the Cu-Hap, the fluorescence
439 spectra suggest the precipitation of an uranium-bearing phase from the autunite family.

440 The spectra of Cu-Hap samples contacted with the mining waters differed from the
441 previous ones (**Figure 7 c**). It is noteworthy that the intensity of the TRFLS signal was much
442 lower than for the samples contacted with synthetic solutions due to lower uranyl loading (**Table**
443 **5**). The positions of the maximum of the peaks were shifted towards the lower wavelengths by
444 about 5 and 2 nm for the samples contacted with V105 and BD200, respectively. For
445 experiments developed with V105, no significant change in the peak position was observed with
446 increasing x_{Cu}. This suggests that the local structure around U(VI) was not significantly different.
447 For BD200, the fluorescence signal was only detected for $x_{Cu} = 0$. Because U loading is similar
448 in all the samples contacted with BD200, the absence of signal for $x_{Cu} > 0$ could be due to the
449 existence of fluorescence quenching effects. Cu^{2+}, among other metal cations, is well known to
450 be a quencher of the U(VI) luminescence in solution[58]. The precise assignment of the spectra
451 recorded for Cu-Hap samples contacted with V105 and BD200 is difficult. It confirms that the
452 mechanism of interaction may be different to that observed when Cu-Hap was contacted with
453 synthetic uranyl solutions.

454

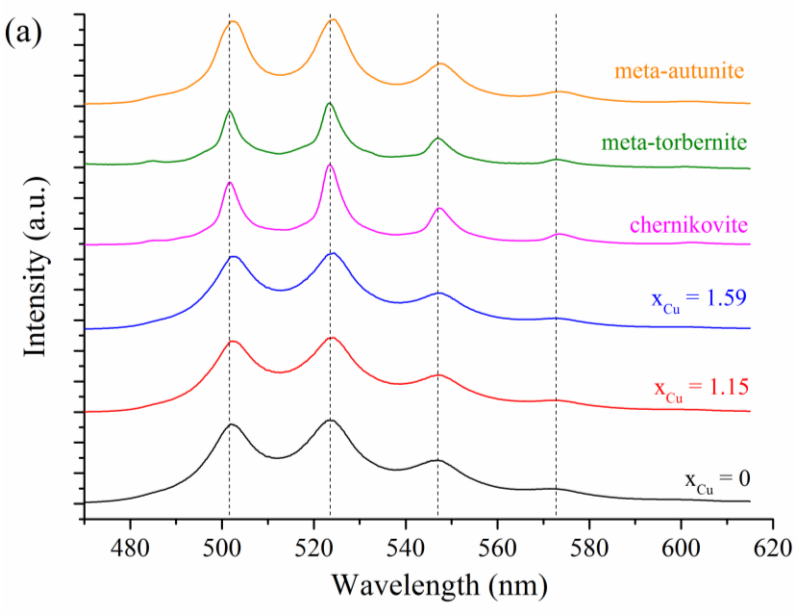
(a)
meta-autunite
meta-torbernite
chernikovite
x_{Cu} = 1.59
x_{Cu} = 1.15
x_{Cu} = 0
Intensity (a.u.)
480
500
520
540
560
580
600
620
Wavelength (nm)

455

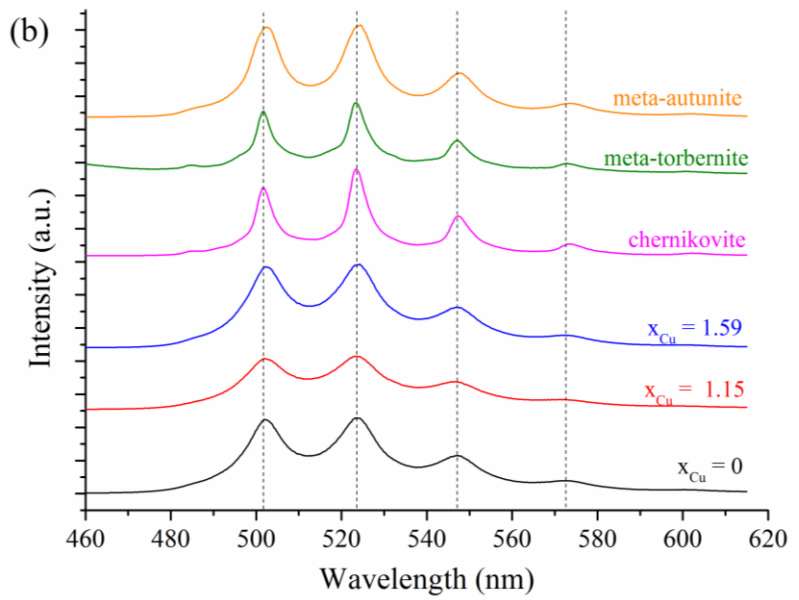
(b)
meta-autunite
meta-torbernite
chernikovite
x_{Cu} = 1.59
x_{Cu} = 1.15
x_{Cu} = 0
Intensity (a.u.)
460
480
500
520
540
560
580
600
620
Wavelength (nm)

456

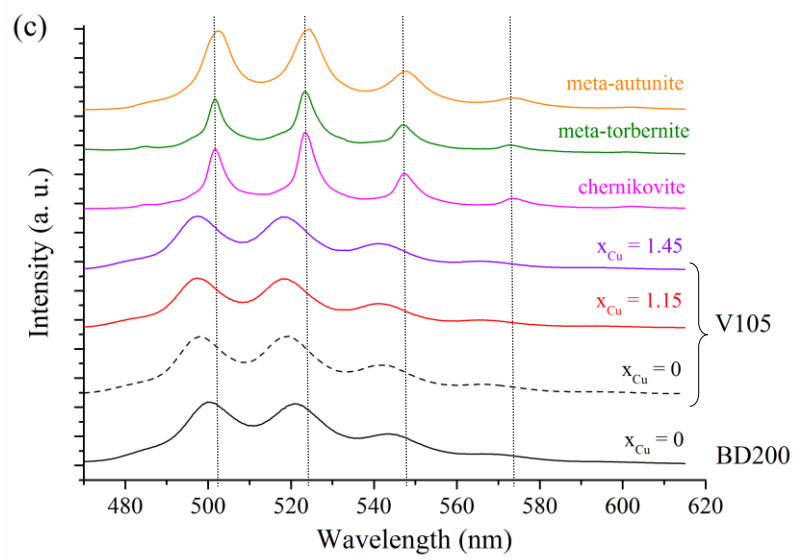

457

458 **Figure 7.** TRLFS spectra of Cu-Hap samples resulting from contact with 0.02 M Na_2SO_4 (a);
459 and 0.02 M $NaNO_3$ (b) synthetic solutions; with BD200 and V105 mining waters (c).
460 The spectra are compared with reference spectra obtained for synthetic meta-
461 torbernite, meta-autunite and chernikovite[59]. Doted lines indicate the position of the
462 maximum of the peaks for the meta-torbernite reference.
463

464 ### 3.4.ENVIRONMENTAL IMPLICATIONS

465 This study demonstrated that Cu-Hap was effective in lowering U concentration when
466 contacting with synthetic solutions or real mining waters. These results showed the high
467 reactivity of the prepared Cu- Hap, which was associated to its poor crystallinity and high
468 specific surface area. Furthermore, the potential carbonate substitution for OH^- and PO_4^{3-} in the
469 Hap lattice is known to increase its solubility and thus its global reactivity[60, 61]. Thus, this
470 material appears as promising in the field of passive treatment devices such as permeable
471 reactive barriers for mining water remediation. Depending on the initial pH and C_U of the mining
472 or doped solutions, several processes were evidenced to support the uranium uptake (**Figure 8**).
473 First, the precipitation of meta-torbernite actually occurred when the bulk solution was
474 oversaturated (case I and II). For V105 (case I), the low pH of the mining water led to the

475 increase of the Cu-Hap solubility. As the S.I. of the bulk solution remained close to equilibrium,
476 the growth of MT crystals was favored. In the second case (synthetic solutions at near neutral
477 pH, case II), oversaturated conditions were reached due to the high uranium concentrations
478 whereas the low solubility of Cu-Hap led to low Cu and P concentrations in solution. As the S.I.
479 of the solutions were highly positive, the nucleation rate was high especially close to the
480 solid/solution interface, leading to the formation of clusters of small crystals covering the surface
481 of the Cu-Hap. These experimental results indicated that precipitation of meta-torbernite can be
482 considered as a potential effective strategy to remove uranium from contaminated water
483 contacted with Cu-Hap. For BD200 mining water (case III), the mechanism for U removal was
484 only speculative. As the bulk solution remained undersaturated, adsorption[4, 5, 12, 15], incorporation
485 in the Cu-Hap structure[28] or combination of both processes[7] were likely to occur.

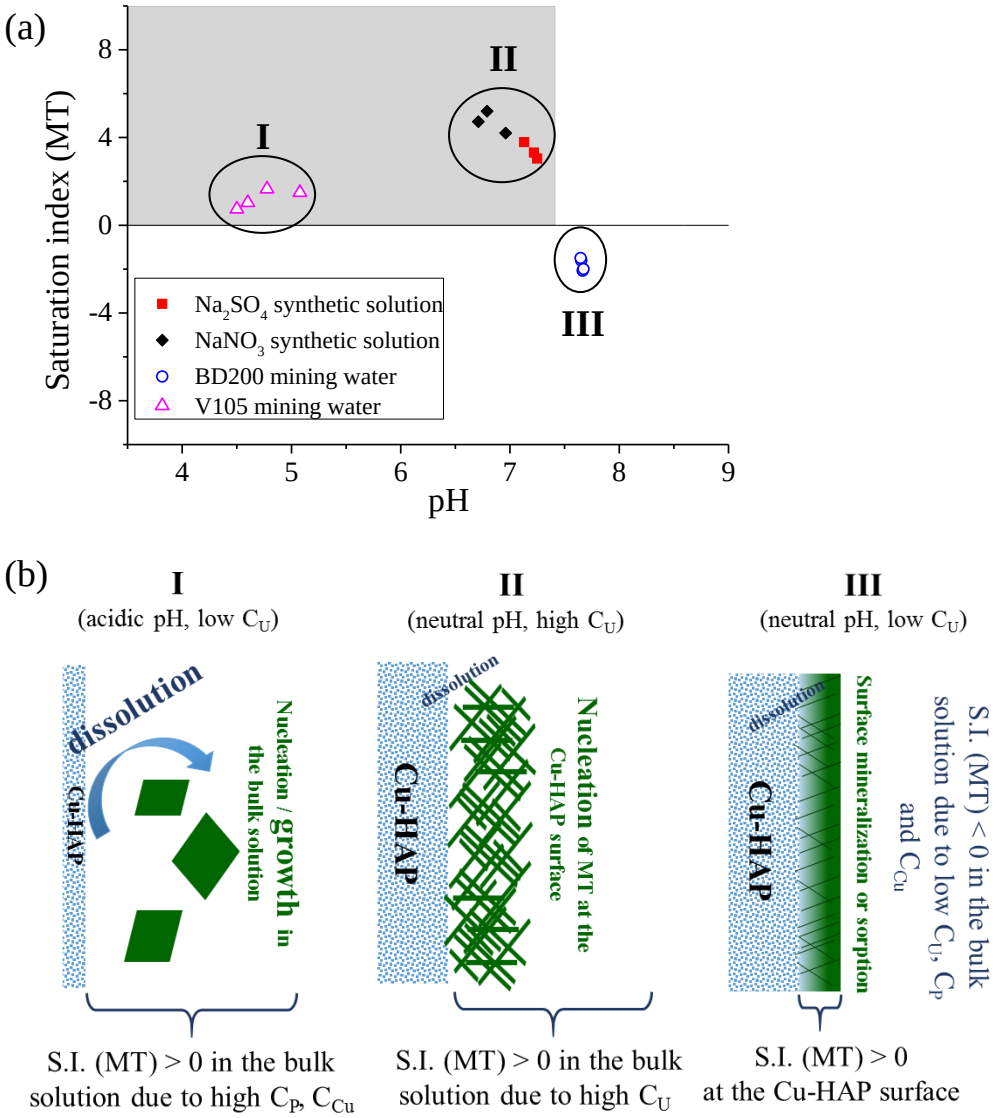

Figure 8. Saturation index of the synthetic solutions and mine waters with respect to meta-torbernite obtained at the end of the batch experiments after contact with Cu-Hap (a). Schematic representation of the three potential processes associated to the uranium uptake (b).

In the absence of Cu and as evidenced by several authors, chernikovite is the precipitating uranium-bearing phase. In order to illustrate the interest of incorporating copper in the Hap, simulations were performed with synthetic 0.02 M $NaNO_3$ and 0.02 M Na_2SO_4 solutions doped with 7.6 µM of uranium, which corresponds to the current French regulatory limit for water

discharges in the environment. Ca, Cu and P concentrations were calculated by dissolving Cu-Hap with x_{Cu} = 1.45 until the solubility of Hap[49] was reached. Using the same selected thermodynamic data[21, 22, 38, 39, 44], the S.I. were calculated in the solutions with respect to meta-torbernite and chernikovite, for pH range representative of most of the mining waters. From these calculations, it is clear that the pH range associated to the precipitation of meta-torbernite is larger than for chernikovite (**Figure 9**). Especially, for 6.7 ≤ pH ≤ 8.2, the solution remained oversaturated regarding to meta-torbernite whereas it was undersaturated regarding to chernikovite. Moreover, meta-torbernite was the most stable phase in the whole pH range. For all the conditions examined, the simulations demonstrated that the precipitation of meta-torbernite could occur in solutions contacted with Cu-Hap, leaving uranium concentration below the regulatory limit in a wide pH range.

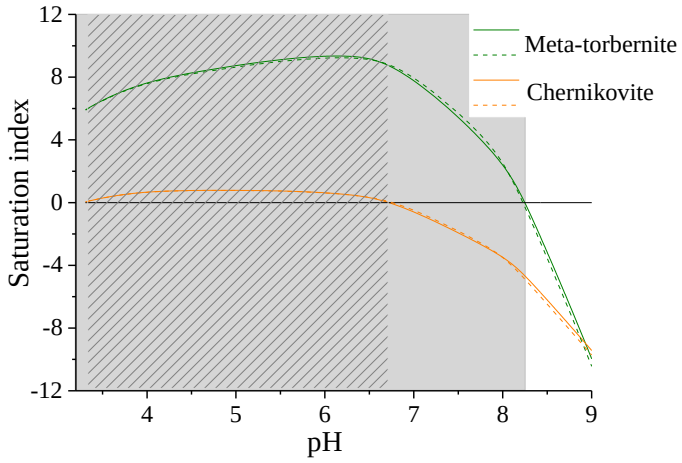

Figure 9. Variation of the saturation index relative to meta-torbernite (MT) and chernikovite (CH) versus pH obtained for a synthetic solution doped with 7.6 µM of uranium. Continuous and dashed lines correspond to 0.02 M $NaNO_3$ and 0.02 M Na_2SO_4 solution, respectively. Gray and hatched areas show the pH range for precipitation of MT and CH, respectively.

To conclude, the main interest for using Cu-Hap is to enlarge the domain of water compositions for which the precipitation of uranyl phosphate is the predominant mechanism

associated to the uranium removal, especially for pH > 6.7 where carbonate uranium species are predominant in the speciation diagrams and pH < 3.3. Fast kinetics of precipitation associated with large field of stability of the meta-torbernite made the formation of meta-torbernite crystals less sensitive to the uranium speciation than for chernikovite or meta-autunite. This mechanism of uranium immobilization led to the formation of crystals, highly enriched in uranium, which could be separated afterwards from the Cu-Hap matrix (e.g. through differential sedimentation). Using this kind of separation process could strongly reduce the amount of contaminated waste to be treated or stored.

Supporting Information. Figure S1 to S6 and Table S1 are available in the supporting information file.

Corresponding Author

*Email: stephanie.szenknect@cea.fr

ACKNOWLEDGMENT

This research was carried out within the framework of a CEA-Orano Mining collaboration and with the precious assistance of people from the Orano Mining Après-Mines France Department (Bessines sur Gartempe, France) to access and sample the mining waters from the Bellezane site.

REFERENCES

1. Naftz, D. L.; Morrison, S. J.; Feltcorn, E. M.; Freethey, G. W.; Fuller, C. C. P., M.J.; Wilhelm, R. G.; R.C., R.; J.A., D.; J.E., B. *Field Demonstration Of Permeable Reactive Barriers To Remove Dissolved Uranium From Groundwater, Fry Canyon, Utah*; 2000.

2. Tokunaga, T. K.; Kim, Y.; Wan, J. M., Potential Remediation Approach for Uranium-Contaminated Groundwaters Through Potassium Uranyl Vanadate Precipitation. *Environ Sci Technol* **2009,** *43*, (14), 5467-5471.
3. Fanizza, M. F.; Yoon, H.; Zhang, C. Y.; Oostrom, M.; Wietsma, T. W.; Hess, N. J.; Bowden, M. E.; Strathmann, T. J.; Finneran, K. T.; Werth, C. J., Pore-scale evaluation of uranyl phosphate precipitation in a model groundwater system. *Water Resources Research* **2013,** *49*, (2), 874-890.
4. Fuller, C. C.; Bargar, J. R.; Davis, J. A., Molecular-scale characterization of uranium sorption by bone apatite materials for a permeable reactive barrier demonstration. *Environ Sci Technol* **2003,** *37*, (20), 4642-4649.
5. Fuller, C. C.; Bargar, J. R.; Davis, J. A.; Piana, M. J., Mechanisms of uranium interactions with hydroxyapatite: Implications for groundwater remediation. *Environ Sci Technol* **2002,** *36*, (2), 158-165.
6. Mehta, V. S.; Maillot, F.; Wang, Z.; Catalano, J. G.; Giammar, D. E., Effect of co-solutes on the products and solubility of uranium(VI) precipitated with phosphate. *Chemical Geology* **2014,** *364*, 66-75.
7. Mehta, V. S.; Maillot, F.; Wang, Z.; Catalano, J. G.; Giammar, D. E., Effect of Reaction Pathway on the Extent and Mechanism of Uranium(VI) Immobilization with Calcium and Phosphate. *Environ Sci Technol* **2016,** *50*, (6), 3128-3136.
8. Mehta, V. S.; Maillot, F.; Wang, Z. M.; Catalano, J. G.; Giammar, D. E., Transport of U(VI) through sediments amended with phosphate to induce in situ uranium immobilization. *Water Research* **2015,** *69*, 307-317.
9. Pan, Z. Z.; Giammar, D. E.; Mehta, V.; Troyer, L. D.; Catalano, J. G.; Wang, Z. M., Phosphate-Induced Immobilization of Uranium in Hanford Sediments. *Environ Sci Technol* **2016,** *50*, (24), 13486-13494.
10. Troyer, L. D.; Maillot, F.; Wang, Z. M.; Wang, Z. M.; Mehta, V. S.; Giammar, D. E.; Catalano, J. G., Effect of phosphate on U(VI) sorption to montmorillonite: Ternary complexation and precipitation barriers. *Geochimica Et Cosmochimica Acta* **2016,** *175*, 86-99.
11. Saldi, G. D.; Daval, D.; Guo, H.; Guyot, F.; Bernard, S.; Le Guillou, C.; Davis, J. A.; Knauss, K. G., Mineralogical evolution of Fe-Si-rich layers at the olivine-water interface during carbonation reactions. *American Mineralogist* **2015,** *100*, (11-12), 2655-2669.
12. Simon, F. G.; Biermann, V.; Peplinski, B., Uranium removal from groundwater using hydroxyapatite. *Applied Geochemistry* **2008,** *23*, (8), 2137-2145.
13. Raicevic, S.; Wright, J. V.; Veljkovic, V.; Conca, J. L., Theoretical stability assessment of uranyl phosphates and apatites: Selection of amendments for in situ remediation of uranium. *Science of the Total Environment* **2006,** *355*, (1-3), 13-24.
14. Lammers, L. N.; Rasmussen, H.; Adilman, D.; deLemos, J. L.; Zeeb, P.; Larson, D. G.; Quicksall, A. N., Groundwater uranium stabilization by a metastable hydroxyapatite. *Applied Geochemistry* **2017,** *84*, 105-113.
15. Arey, J. S.; Seaman, J. C.; Bertsch, P. M., Immobilization of uranium in contaminated sediments by hydroxyapatite addition. *Environ Sci Technol* **1999,** *33*, (2), 337-342.
16. Kong, L.; Ruan, Y.; Zheng, Q.; Su, M.; Diao, Z.; Chen, D.; Hou, L. a.; Chang, X.; Shih, K., Uranium extraction using hydroxyapatite recovered from phosphorus containing waste water. *Journal of Hazardous Materials* **2020,** *382*, 120784.
17. Su, M.; Tsang, D. C. W.; Ren, X.; Shi, Q.; Tang, J.; Zhang, H.; Kong, L.; Hou, L. a.; Song, G.; Chen, D., Removal of U(VI) from nuclear mining effluent by porous hydroxyapatite:

583 Evaluation on characteristics, mechanisms and performance. *Environmental Pollution* **2019,** *254*,
584 112891.
585 18. Dzik, E. A.; Lobeck, H. L.; Zhang, L.; Burns, P. C., Thermodynamic properties of
586 phosphate members of the meta-autunite group: A high-temperature calorimetric study. *Journal*
587 *of Chemical Thermodynamics* **2017,** *114*, 165-171.
588 19. Jerden Jr, J. L.; Sinha, A. K., Phosphate based immobilization of uranium in an oxidizing
589 bedrock aquifer. *Applied Geochemistry* **2003,** *18*, (6), 823-843.
590 20. Gorman-Lewis, D.; Burns, P. C.; Fein, J. B., Review of uranyl mineral solubility
591 measurements. *Journal of Chemical Thermodynamics* **2008,** *40*, (3), 335-352.
592 21. Gorman-Lewis, D.; Shvareva, T.; Kubatko, K. A.; Burns, P. C.; Wellman, D. M.;
593 McNamara, B.; Szymanowski, J. E. S.; Navrotsky, A.; Fein, J. B., Thermodynamic Properties of
594 Autunite, Uranyl Hydrogen Phosphate, and Uranyl Orthophosphate from Solubility and
595 Calorimetric Measurements. *Environ Sci Technol* **2009,** *43*, (19), 7416-7422.
596 22. Cretaz, F.; Szenknect, S.; Clavier, N.; Vitorge, P.; Mesbah, A.; Descostes, M.; Poinssot,
597 C.; Dacheux, N., Solubility properties of synthetic and natural meta-torbernite. *Journal of*
598 *Nuclear Materials* **2013,** *442*, (1-3), 195-207.
599 23. Vesely, V.; Pekarek, V.; Abbrent, M., A study of uranyl phosphates. 3. Solubility
600 products of uranyl hydrogen phosphate uranyl orthophosphate and some alkali uranyl
601 phosphates. *J Inorg Nucl Chem* **1965,** *27*, (5), 1159-1166.
602 24. Pekarek, V.; Vesely, V.; Ullrich, J., Synthetic double phosphates of uranyl with divalent
603 cations - Solubility and some physico-chemical properties. *Bulletin De La Societe Chimique De*
604 *France* **1968**, 1844-&.
605 25. Ilton, E. S.; Zachara, J. M.; Moore, D. A.; McKinley, J. P.; Eckberg, A. D.; Cahill, C. L.;
606 Felmy, A. R., Dissolution Study of Metatorbernite: Thermodynamic Properties and the Effect of
607 pH and Phosphate. *Environ Sci Technol* **2010,** *44*, (19), 7521-7526.
608 26. Van Haverbeke, L.; Vochten, R.; Van Springel, K., Solubility and spectrochemical
609 characteristics of synthetic chernikovite and meta-ankoleite. *Mineralogical Magazine* **1996,** *60*,
610 (5), 759-766.
611 27. Schindler, M.; Durocher, J. L.; Kotzer, T. G.; Hawthorne, F. C., Uranium-bearing phases
612 in a U-mill disposal site in Northern Canada: Products of the interaction between
613 leachate/raffinate and tailings material. *Applied Geochemistry* **2013,** *29*, 151-161.
614 28. Ohnuki, I.; Kozai, N.; Samadfam, M.; Yasuda, R.; Yamamoto, S.; Narumi, K.; Naramoto,
615 H.; Murakami, T., The formation of autunite ($Ca(UO_2)_2(PO_4)_2$. nH_2O)within the leached layer of
616 dissolving apatite: incorporation mechanism of uranium by apatite. *Chemical Geology* **2004,**
617 *211*, (1-2), 1-14.
618 29. Rakovan, J.; Reeder, R. J.; Elzinga, E. J.; Cherniak, D. J.; Tait, C. D.; Morris, D. E.,
619 Structural characterization of U(VI) in apatite by X-ray absorption spectroscopy. *Environ Sci*
620 *Technol* **2002,** *36*, (14), 3114-3117.
621 30. Shanmugam, S.; Gopal, B., Copper substituted hydroxyapatite and fluorapatite:
622 Synthesis, characterization and antimicrobial properties. *Ceramics International* **2014,** *40*, (10),
623 15655-15662.
624 31. Tounsi, H.; Djemal, S.; Petitto, C.; Delahay, G., Copper loaded hydroxyapatite catalyst
625 for selective catalytic reduction of nitric oxide with ammonia. *Applied Catalysis B:*
626 *Environmental* **2011,** *107*, (1–2), 158-163.

627 32. Li, C.; Ge, X.; Zhao, J.; Li, G.; Bai, J.; Du, Q.; Ding, R., Preparation and characterization
628 of novel hydroxyapatite/copper assemblies with well-defined morphologies. *Solid State Sciences*
629 **2014,** *29*, 66-74.
630 33. Li, Y.; Ho, J. H.; Ooi, C. P., Antibacterial efficacy and cytotoxicity studies of copper (II)
631 and titanium (IV) substituted hydroxyapatite nanoparticles. *Materials Science & Engineering C-*
632 *Materials for Biological Applications* **2010,** *30*, (8), 1137-1144.
633 34. Stanic, V.; Dimitrijevic, S.; Antic-Stankovic, J.; Mitric, M.; Jokic, B.; Plecas, I. B.;
634 Raicevic, S., Synthesis, characterization and antimicrobial activity of copper and zinc-doped
635 hydroxyapatite nanopowders. *Applied Surface Science* **2010,** *256*, (20), 6083-6089.
636 35. Liu, G.; Talley, J. W.; Na, C. Z.; Larson, S. L.; Wolfe, L. G., Copper Doping Improves
637 Hydroxyapatite Sorption for Arsenate in Simulated Groundwaters. *Environ Sci Technol* **2010,**
638 *44*, (4), 1366-1372.
639 36. Wallaeys, R., Contribution à l'études des apatites phosphocalciques. *Annales de Chimie*
640 **1952,** *7*, 808-848.
641 37. Parkhurst, D. H.; Appelo, C. A. J. *User's Guide to PHREEQC (Version 2) - A Computer*
642 *Program for Speciation, Batch-Reaction, One-Dimensional Transport, and Inverse Geochemical*
643 *Calculations*; U.S.G.S Water-Resources Investigations Report 99-4259: 1999.
644 38. Giffaut, E.; Grivé, M.; Blanc, P.; Vieillard, P.; Colàs, E.; Gailhanou, H.; Gaboreau, S.;
645 Marty, N.; Madé, B.; Duro, L., Andra thermodynamic database for performance assessment:
646 ThermoChimie. *Applied Geochemistry* **2014,** *49*, 225-236.
647 39. Grivé, M.; Duro, L.; Colàs, E.; Giffaut, E., Thermodynamic data selection applied to
648 radionuclides and chemotoxic elements: An overview of the ThermoChimie-TDB. *Applied*
649 *Geochemistry* **2015,** *55*, 85-94.
650 40. Reiller, P. E.; Descostes, M., Building and Application of the Thermodynamic Database
651 PRODATA, Dedicated to Mining and Environmental Monitoring Activities. *Submitted in*
652 *Chemosphere* **2019**.
653 41. Frontera, C.; Rodriguez-Carvajal, J., FullProf as a new tool for flipping ratio analysis.
654 *Physica B: Condensed Matter* **2003,** *335*, (1-4), 219-222.
655 42. Thompson, P.; Cox, D. E.; Hastings, J. B., Rietveld Refinement of Debye-Scherrer
656 Synchrotron X-Ray Data from Al_2O_3 *Journal of Applied Crystallography* **1987,** *20*, 79-83.
657 43. Othmane, G.; Allard, T.; Vercouter, T.; Morin, G.; Fayek, M.; Calas, G., Luminescence
658 of uranium-bearing opals: Origin and use as a pH record. *Chemical Geology* **2016,** *423*, 1-6.
659 44. Allison, J. D.; Brown, D. S.; Novo-Grada, K. J., MINTEQA2/PRODEFA2 - A
660 Geochemical Assessment Model for Environmental Systems - Version 3.0 User's Manual:
661 Environmental Research Laboratory. *Office of Resaerch Athens, Georgia.* **1990**.
662 45. Gomes, S.; Nedelec, J.-M.; Jallot, E.; Sheptyakov, D.; Renaudin, G., Unexpected
663 Mechanism of Zn2+ Insertion in Calcium Phosphate Bioceramics. *Chemistry of Materials* **2011,**
664 *23*, (12), 3072-3085.
665 46. Karpov, A. S.; Nuss, J.; Jansen, M.; Kazin, P. E.; Tretyakov, Y. D., Synthesis, crystal
666 structure and properties of calcium and barium hydroxyapatites containing copper ions in
667 hexagonal channels. *Solid State Sciences* **2003,** *5*, (9), 1277-1283.
668 47. Antonakos, A.; Liarokapis, E.; Leventouri, T., Micro-Raman and FTIR studies of
669 synthetic and natural apatites. *Biomaterials* **2007,** *28*, (19), 3043-3054.
670 48. O'Donnell, M. D.; Fredholm, Y.; de Rouffignac, A.; Hill, R. G., Structural analysis of a
671 series of strontium-substituted apatites. *Acta Biomaterialia* **2008,** *4*, (5), 1455-1464.

672 49. Nancollas, G. H., The nucleation and growth of phosphate minerals. In *Phosphate*
673 *Minerals*, Nriagu, J. O.; Moore, P. B., Eds. Springer-Verlag: Berlin, 1984; pp 137-154.
674 50. Munasinghe, P. S.; Elwood Madden, M. E.; Brooks, S. C.; Elwood Madden, A. S.,
675 Dynamic interplay between uranyl phosphate precipitation, sorption, and phase evolution.
676 *Applied Geochemistry* **2015,** *58*, 147-160.
677 51. Frost, R. L., An infrared and Raman spectroscopic study of the uranyl micas.
678 *Spectrochimica Acta Part a-Molecular and Biomolecular Spectroscopy* **2004,** *60*, (7), 1469-
679 1480.
680 52. Singh, A.; Ulrich, K. U.; Giammar, D. E., Impact of phosphate on U(VI) immobilization
681 in the presence of goethite. *Geochimica Et Cosmochimica Acta* **2010,** *74*, (22), 6324-6343.
682 53. Baumann, N.; Arnold, T.; Foerstendorf, H.; Read, D., Spectroscopic Verification of the
683 Mineralogy of an Ultrathin Mineral Film on Depleted Uranium. *Environ Sci Technol* **2008,** *42*,
684 (22), 8266-8269.
685 54. Wang, Z.; Zachara, J. M.; Liu, C.; Gassman, P. L.; Felmy, A. R.; Clark, S. B., A
686 cryogenic fluorescence spectroscopic study of uranyl carbonate, phosphate and oxyhydroxide
687 minerals. *Radiochimica Acta* **2008,** *96*, (9-11), 591-598.
688 55. Locock, A. J.; Burns, P. C., Crystal structures and synthesis of the copper-dominant
689 members of the autunite and meta-autunite groups: Torbernite, zeunerite, metatorbernite and
690 metazeunerite. *Canadian Mineralogist* **2003,** *41*, 489-502.
691 56. Locock, A. J.; Burns, P. C., The crystal structure of synthetic autunite, $Ca(UO_2)(PO_4)$.
692 $2(H_2O)$. *American Mineralogist* **2003,** *88*, (1), 240-244.
693 57. Locock, A. J.; Burns, P. C.; Duke, M. J. M.; Flynn, T. M., Monovalent cations in
694 structures of the meta-autunite group. *Canadian Mineralogist* **2004,** *42*, 973-996.
695 58. Maji, S.; Sundararajan, K.; Viswanathan, K. S., Correction for quenching in fluorimetric
696 determinations using steady state fluorescence. *Spectrochimica Acta Part a-Molecular and*
697 *Biomolecular Spectroscopy* **2000,** *56*, (7), 1251-1256.
698 59. Crétaz, F. Etude de la solubilité et des cinétiques de dissolution des phosphates et
699 vanadates d'uranium : Implications pour l'amont du cycle électronucléaire. Université
700 Montpellier II, 2013.
701 60. Kolmas, J.; Piotrowska, U.; Kuras, M.; Kurek, E., Effect of carbonate substitution on
702 physicochemical and biological properties of silver containing hydroxyapatites. *Materials*
703 *Science and Engineering: C* **2017,** *74*, 124-130.
704 61. Moore, R. C.; Rigali, M. J.; Brady, P., Selenite sorption by carbonate substituted apatite.
705 *Environmental Pollution* **2016,** *218*, 1102-1107.

706